Article, Published Version

Schulz, Kirstin; Burchard, Hans; Mohrholz, Volker; Holtmsann, Peter; Schuttelaars, Henk M.; Becker, Marius; Maushake, Christian; Gerkema, Theo

Intratidal and spatial variability over a slope in the Ems estuary: Robust along-channel SPM transport versus episodic events

Estuarine, Coastal and Shelf Science

Estuarine, Coastal and Shelf Science 243 (2020) 106902

Contents lists available at ScienceDirect

Estuarine, Coastal and Shelf Science

journal homepage: http://www.elsevier.com/locate/ecss

Intratidal and spatial variability over a slope in the Ems estuary: Robust along-channel SPM transport versus episodic events

Kirstin Schulz [a,f], Hans Burchard [b], Volker Mohrholz [b], Peter Holtermann [b], Henk M. Schuttelaars [c], Marius Becker [d], Christian Maushake [e], Theo Gerkema [f,*]

[a] Alfred Wegener Institute, Helmholtz Centre for Polar and Marine Research, Bremerhaven, Germany
[b] Leibniz Institute for Baltic Sea Research Warnemünde, Seestraße 15, D-18119 Rostock, Germany
[c] Delft Institute of Applied Mathematics, Delft University of Technology, Van Mourik Broekmanweg 6, 2628 XE Delft, the Netherlands
[d] Kiel University, Institute of Geosciences, Otto-Hahn-Platz 1, 24118 Kiel, Germany
[e] BAW - Federal Waterways Engineering and Research Institute, Hamburg, Germany
[f] NIOZ Netherlands Institute for Sea Research, Department of Estuarine and Delta Systems, and Utrecht University, P.O. Box 140, 4400 AC Yerseke, the Netherlands

ARTICLE INFO

Keywords:
Lateral circulation
SPM transport
Ems estuary
EDoM18

ABSTRACT

Results from measurements are presented that were collected during a full tidal cycle in the Ems estuary, involving two landers and an anchored research vessel. The conditions were characterized by very weak winds, no wave effects, and low river run-off, so that the state was close to tide-only. We find that the lateral (i.e., cross-slope) transport of water and suspended particulate matter (SPM) much of the time shows a vertically layered structure, which is however subject to sudden transitions. Moreover, even on the small spatial scale of these measurements (i.e., within a distance of 200 m), a strong lateral variability is observed in the circulation patterns. We analyze its dynamics by means of dimensionless parameters. In addition, near-bottom peaks in SPM concentration are observed, notably during early flood. However, these episodic events have little effect on the overall transport of SPM, which involves the whole water column: the measurements show a high vertically integrated SPM signal during late ebb, resulting in an ebb-dominance in the transport at this position in the tidal channel.

1. Introduction

Estuaries, connecting the riverine and marine environment, can be efficient traps for marine and fluvial sediments, resulting in localized regions of high suspended sediment concentrations, a so-called estuarine turbidity maximum (ETM) (Burchard et al., 2018). The observed concentrations and specific trapping locations can be strongly influenced by human interventions, such as land reclamation (Van Maren et al., 2016), construction of weirs (Schuttelaars et al., 2013), dredging activities and channel deepening (Chernetsky et al., 2010; De Jonge et al., 2014; Dijkstra et al., 2019a), and water quality improvements (Cox et al., 2019). These changes, especially when the observed concentrations strongly increase, can adversely affect both the economic and ecological value of estuaries: shipping channels have to be dredged to allow (ever larger) vessels to reach ports, and light penetration and availability of oxygen in the water are reduced, thus negatively impacting the ecology (De Jonge and Schückel, 2019). Therefore, insight into the effects of human interventions is essential for a proper management of the estuarine systems.

A system where such a regime shift from low to high sediment concentrations was observed after deepening of the fairway is the Ems River (upper estuary) (Dijkstra et al., 2019b), one of four distinct regions that make up the Ems–Dollard estuary (see Fig. 1). Along with increasing concentration, the ETM moved upstream and widened considerably (Talke et al., 2009; De Jonge et al., 2014).

However, both the impact of the fairway deepening on the turbidity levels in the lower and middle reaches and Dollard, and the influence of land reclamation remain poorly understood. One of the main reasons is the complexity of the three dimensional hydrodynamics and sediment dynamics in the region where the Ems river (upper estuary), the Dollard (a shallow region separated from the Ems river by the Geiseleitdamm) and the middle reaches interact: the connection between these parts of the system is poorly understood, as are the pathways of suspended sediment.

* Corresponding author.
E-mail address: theo.gerkema@nioz.nl (T. Gerkema).

https://doi.org/10.1016/j.ecss.2020.106902
Received 19 March 2020; Received in revised form 6 June 2020; Accepted 19 June 2020
Available online 8 July 2020

On August 28, 2018, the joint German-Dutch campaign *EDoM'18* took place involving eight research vessels at different locations, between Eemshaven and Papenburg (not shown). As part of this effort, the NIOZ research vessel Navicula was anchored at the position indicated in Fig. 1 (red dot) to carry out 13-h measurements, involving two bottom landers at both sides of the ship over the southwestern slope. These observations are presented and analyzed here, with the central aim to estimate the along-channel SPM transport at this location. Before and during the campaign, the wind was very weak and hence there were no wave effects; moreover, the river run-off is relatively low in this time of year. So the conditions were close to tide-only and we expect the tides to be the dominant factor in the dynamics.

In Section 2 we present the background information on the measurement site, conditions during the measurements, and the instruments. In Section 3 we present the results, including a comparison with nearby long-term data, an analysis of residual circulation and SPM transport, near-bottom bursts of high SPM, and the spatial and temporal variability of the lateral circulation. Finally, in Section 4 we present a discussion and conclusions.

2. Setting of measurements

A map of the Ems estuary is shown in Fig. 1; measurements were carried out on August 28, 2018, at the location indicated by the red dot. In more detail, Fig. 2 shows the positions of the landers and the anchor station.

2.1. Study area and background conditions

As visible in Fig. 3a, the survey campaign took place during very calm conditions, with wind speeds below 4 m s^{-1}. No wind waves were present during the campaign, and air temperature ranged from 14 to 20°C (Fig. 3b). The survey coincided with spring tides (full moon was on 26 August 2018). The river discharge from the Ems is, as typically in this time of year, very low. The daily averaged discharge reported at the monitoring station in Versen (100 km upstream of the measurement location) on August 28 was 22 m^3 s^{-1}, which is much smaller than the annual-mean daily discharge of 80 m^3 s^{-1} (source: Wasserstraßen-und Schifffahrtsverwaltung des Bundes (WSV), provided by Bundesanstalt für Gewässerkunde (BfG)). For an indication on how the discharge at Versen relates to the overall discharge, in a long-term mean sense, we refer to Van Beusekom and De Jonge (1998).

The measurements started and ended around low waters, but it is to be noted that the first low water was 0.5 m higher than the second. This considerable difference between successive low waters is not found in a tidal reconstruction of the signal (not shown), and only weak winds were present during the day. A possible explanation might be that westerly winds during the previous day (see Fig. 3a) created higher water levels and that our first low water is a holdover of this episode. More generally, by examining water-level anomalies against wind strength and direction for a longer period, we find that southwesterly to northwesterly winds create higher water levels, while they are lower for northeasterly to southeasterly winds.

2.2. Instrumentation

Two moorings were deployed in the early morning of August 28, one on the southwestern channel-slope (at 53°18.996′N, 07°01.026′E, referred to as "IOW mooring" in the following), and one further into the channel (at 53°19.092'N, 07°01.086′E, "NIOZ mooring" in the following). The ship was subsequently anchored between the two moorings (each at about a 100 m distance) and 13 hours of measurements were performed to sample a whole tidal cycle, before recovering the moorings again in the evening. The exact positions of the moorings and the ship are indicated in Fig. 2.

The NIOZ mooring was equipped with an Acoustic Doppler Current

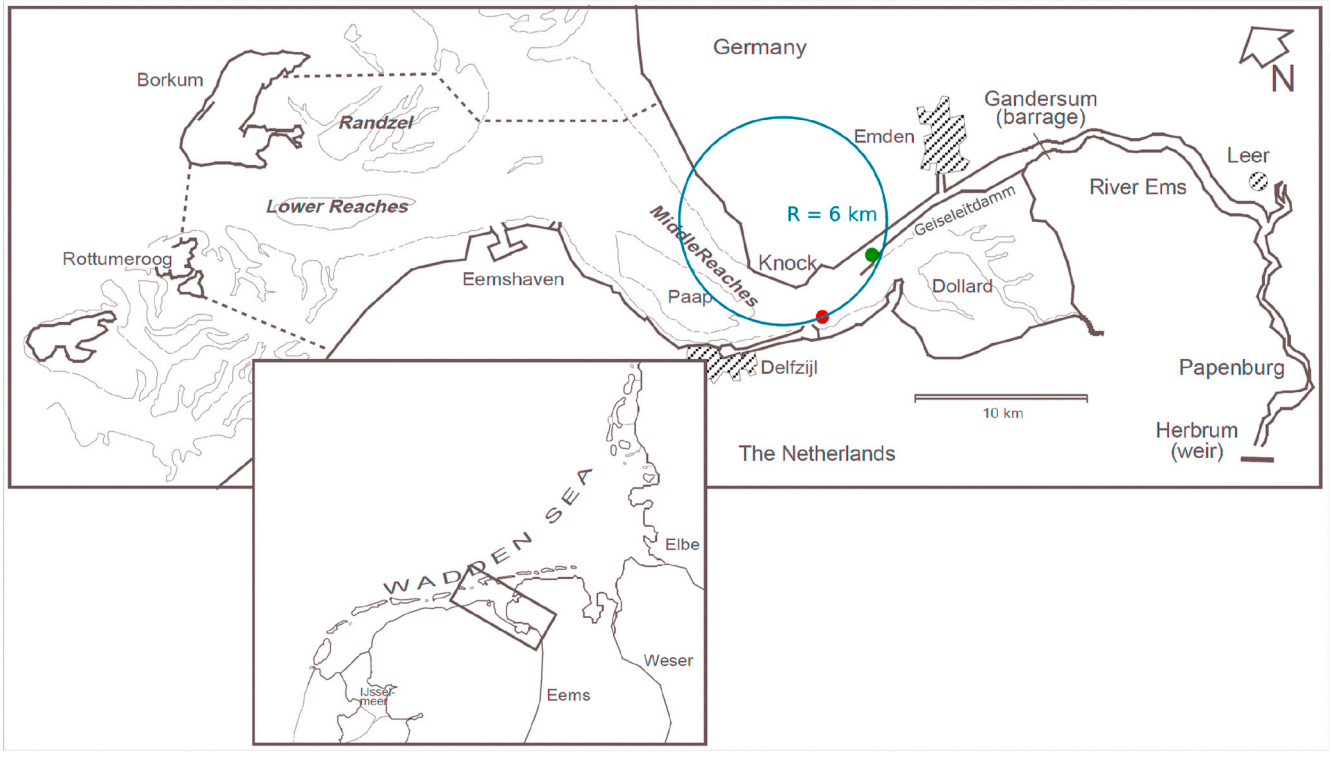

Fig. 1. Map of the Ems estuary with a subdivision in four main areas (lower reaches, middle reaches, Dollard and upper estuary/Ems River), adopted from De Jonge et al. (2014). The red dot indicates the principal measurement site, the blue circle the approximate channel curvature with radius R at that position. The green dot indicates another measurement site ~ 5 km upstream (used in Section 3.3). (For interpretation of the references to color in this figure legend, the reader is referred to the Web version of this article.)

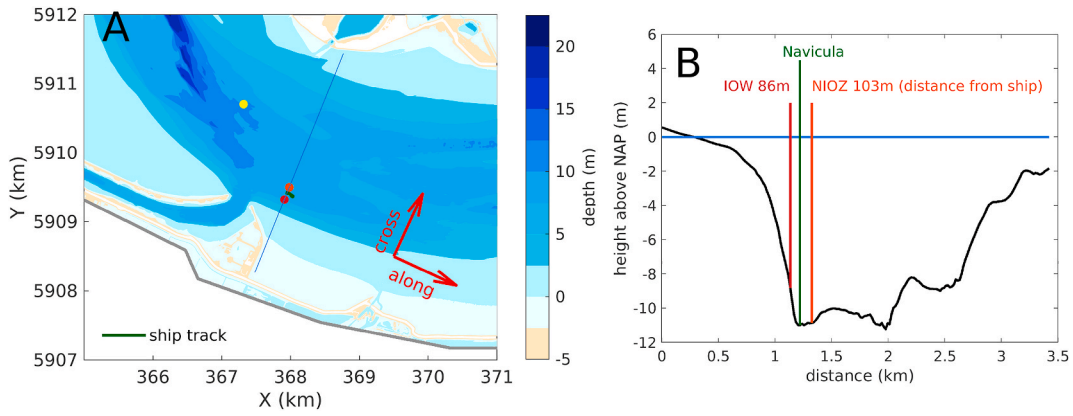

Fig. 2. (a) Bathymetric map of the study area with positions of the IOW-moorings (red dot), the NIOZ-mooring (orange dot), and the drift track of the anchored ship (green line) in-between. The yellow dot indicates the position of the long-term mooring. Coordinates are in UTM32 (UTM stands for Universal Transverse Mercator). (b) Cross-channel transect (along the blue line in (a)), again with (short-term) mooring and ship positions indicated. (For interpretation of the references to color in this figure legend, the reader is referred to the Web version of this article.)

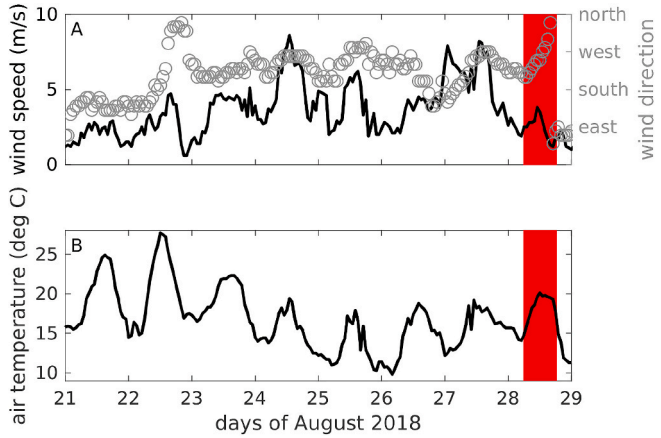

Fig. 3. Time series of (a) wind speed (solid line) and direction (gray circles), and (b) air temperature, both measured at the DWD station in Emden. Red patches mark the time of the ship survey. (For interpretation of the references to color in this figure legend, the reader is referred to the Web version of this article.)

Profiler (ADCP), a turbidity sensor and a submersible laser-diffraction based particle size analyzer (LISST-200X, Sequoia Scientific, Inc.). The turbidity sensor (Infinity-Turbi, JFE) was mounted at a height of 0.34 m above the bottom of the frame. Data was sampled at bursts of 5 min, with 295 samples per burst. After every burst, a mechanical wiper cleaned the optical window. The instrument was also equipped with a temperature sensor.

Current velocity profiles were obtained with a bottom mounted (upward facing) 1 MHz ADCP (Signature 1000 from Nortek AS), measuring with a frequency of 8 Hz in bursts of 1 s. The bin size was set to 0.2 m with a blanking distance of 0.1 m and a mounting height of approximately 0.52 m. This allowed the ADCP to sample the water column from 0.72 m above the bottom to the surface.

The LISST-200X was mounted horizontally on the NIOZ mooring at a height of approximately 0.30 m above the seabed. A path reduction module (PRM) was installed to reduce the optical path to 5 mm, as highly turbid water was expected. The sampling rate was set to 60 s, for each measurement 20 samples were averaged automatically.

The IOW mooring consisted of a stainless steel bottom frame with an upward looking ADCP, a SBE37 thermosalinometer and a PME MiniDOT oxygen optode. The 1.2 Mhz Workhorse-ADCP was used in mode 12 to combine a high sampling frequency with high accuracy. Every 2 s a set of nine subpings was averaged into a single profile and stored. The special beam angle of 54° prevented a blind side lobe range at the surface, and allowed the concurrent estimation of turbulent kinetic energy (TKE) and its dissipation, using the variance method. Oxygen measurements were taken 0.15 m above the bottom with 60 s sampling interval. The SBE37 was mounted 20 cm above the bottom. The sampling interval was 15 s. All devices at the mooring were calibrated prior to the cruise in the IOW calibration lab.

Ship based measurements included permanent profiling with a microstructure probe, a vessel-mounted ADCP, and continuous surface conductivity and temperature sampling. The Microstructure Profiler (MSS 90-S) was used for simultaneous microstructure and precision measurements of physical parameters in the entire water column. The profiler was equipped with two velocity shear sensors, a fast temperature sensor (FP07), standard sensors for conductivity, temperature, depth (CTD); oxygen and turbidity measurements. All sensors were mounted at the head of the profiler. The sampling rate was 1024 Hz. The profiler was used in free fall mode with a downward velocity of approximately 0.6 m s^{-1}. The TKE dissipation rate was calculated by fitting the observed shear spectrum to the theoretical Nasmyth spectrum in a wave number range from 2 to maximum 30 cycles per meter.

A Seabird SBE 19 plus CTD was mounted on a pole attached to the ship, approximately 1 m below the water surface, sampling continuously at a resolution of 4 Hz.

On the same pole, a downward-facing 1.2 kHz RDI Workhorse ADCP was mounted. The bin size was set to 0.5 m, profiles were taken from 1.5 m below the surface (including the 0.25 m blanking distance) in intervals of 3 s and afterwards averaged to 5 min intervals.

In addition to the short-term measurements (covering one tidal cycle), a "long-term" mooring was placed at the position of the yellow dot in Fig. 2 (53°19.730'N, 07°00.459'E), between August 8 and September 5. On this mooring, an optical backscatter sensor (OBS) and an upward-looking 600 kHz ADCP were mounted, at a height of 0.8 m above the river bed. The ADCP bin size was 0.5 m. The ping rate was 0.2 Hz, with 6 sub-pings averaged. Beam velocities were converted to earth coordinates during acquisition. For further processing, current velocities were averaged in intervals of 1 min and projected onto the direction of the flood current. Data close to (i.e. 1.2 m below) the water surface was biased and omitted for calculating depth averaged velocity.

2.3. SPM calibration

To translate the optical backscatter data to values of SPM concentration, two water samples using a Niskin bottle were taken approximately every 20 min, one near the surface and one near the bottom.

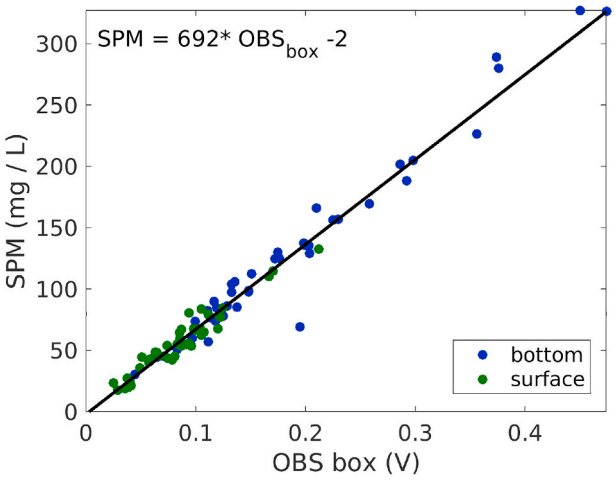

Fig. 4. Scatter plot of turbidity (obtained with an OBS in a dark box) vs. measured SPM concentration (obtained from filtration), and the linear fit obtained with the Theil-Sen regression.

Subsamples were filtered on dried and pre-weighed GF/F filters, which were subsequently rinsed and again dried and weighed to obtain the concentration of SPM. Simultaneously, OBS values for the same water sample were obtained using an OBS sensor in a dark box on board of the ship. In total, 82 samples were taken. A linear regression between the two data sets was obtained with the Theil-Sen method, which is less sensitive to outliers and therefore more appropriate in this context than the least squares fit (Gerkema et al., 2014; Schulz and Gerkema, 2018). The data and regression are displayed in Fig. 4.

In a second step, the OBS in the dark box was inter-calibrated with the turbidity sensors on the microstructure profiler (from IOW). For this purpose, a dilution series of bottom water, sampled at peak turbidity during ebb phase, was performed after the measurements on August 28. The sampled water with high SPM concentration was concurrently measured in a bucket with the MSS and the OBS, while the water was stirred to maintain a uniform SPM concentration. After dilution with pure water the measurement was repeated. In all cases, five dilution steps were performed. After calibration of the OBS with the SPM samples, the MSS turbidity sensor readings were calibrated with the corrected OBS values. The calculation of SPM concentration from the MSS turbidity sensor readings was performed using the fit:

$$\mathrm{SPM\_concentration[mg/l]} = 1.60 \times \mathrm{MSS\_turbidity[NTU]}^{0.949}.$$

An inter-calibration of the moored Infinity turbidity sensor (NIOZ mooring) with the OBS in the dark box had been performed at a previous occasion (in November 2017), resulting in the linear regression of $\mathrm{OBS}_{box} = 0.0033 \times \mathrm{FTU}_{\infty} - 0.12$.

3. Results

3.1. Tidal characteristics over an extended period

The campaign results described in this paper encompass just one tidal cycle, so naturally the question arises how representative the data is for the typical state in that time of year. To examine this, we analyzed data from the long-term mooring (see end of Section 2.2), deployed approximately 1 km downstream from our position (yellow dot in Fig. 2a) during the period 8 August - 5 September 2018, which includes the tidal cycle of our campaign. In total, 45 full tidal cycles were covered; they are all individually plotted in Fig. 5, with slack tides (from ebb to flood) synchronized in each cycle and set at $t = 0$. The following key quantities are shown: sea surface elevation (from a nearby tide gauge, Knock, data courtesy of WSA, Wasserstraßen-und Schifffahrtsamt Emden) along-channel current velocity (U), and turbidity. Neap tides (blue) and spring tides (red) are indicated; the mean of all cycles is plotted in black.

A remarkable feature in the along-channel current is the very early occurrence of maximum flood velocities: the flood current is (on average) strongest approximately 1 h after slack tide (Fig. 5b). This early maximum is most pronounced during spring tides, and is also reflected in the turbidity record (Fig. 5c). For most of the recorded tidal cycles, *two* local turbidity peaks (I and II in Fig. 5b) are visible during the first hours of flood. This means that there is not a one-to-one relation with the onset of flood (which has only one peak), suggesting that other mechanisms are at work besides local resuspension, e.g., lateral advection. It should be stressed that these peaks were measured near the bottom (i.e., at a height of about 0.8 m). With regard to total mass transport of sediment (i.e., integrated over the whole water column), these peaks may be a 'red herring', in the sense that their near-bottom flood transport, while locally high, contributes little to the overall vertically integrated transport. This, at least, is suggested by the ship measurements discussed below.

Subsequently, the turbidity decays and, on average, remains nearly constant throughout the flood phase. During some tidal cycles, the turbidity is again enhanced towards the end of the flood phase (peak III). A clear drop in turbidity occurs during slack tides.

Peak ebb velocities also occur early in the tidal cycle, but the deviation from a sinusoidal tide is much less pronounced than during flood phase. A corresponding increase in turbidity can be observed (peak IV), after which the level of turbidity is again constant. Strikingly, the maximum turbidity during ebb is persistently recorded towards the end of the ebb phase (peak V), when current velocities are already decreasing. This suggests a source of sediment further upstream, that is resuspended during full ebb flow and subsequently transported downstream. But, again, the full water column should be considered to warrant such conclusions, as further discussed below.

The cycle coinciding with our ship measurements is indicated by the green line in Fig. 5. It is fairly close to the mean state (black line), but with slightly higher current and turbidity values, as is to be expected during spring-tide conditions. All in all, we can conclude that our measurements are representative for the summer period covered by the lander.

3.2. Stratification and mixing

Turning now to the measurements made on August 28, we first consider the data from the NIOZ lander (Fig. 2b). From its ADCP, the along and cross-channel current velocities are obtained, see Fig. 6a and b. Like in Fig. 5, we find a clear peak at early flood (in red), while the ebb phase (blue) is more uniform. The behavior of the cross-channel current is much more intricate. Much of the time, a two-layer structure is observed, with upslope currents (blue) on top and downslope current (red) below – or vice versa. The transition between these states (or an occasional state of vertical uniformity) is abrupt. In section 3.5 we discuss the lateral circulation at more length.

Also shown are the isopycnals (black contours, Fig. 6, all panels). They show the classical picture of a strain-induced periodic stratification (Simpson et al., 1990): destratification in the course of flood, and a built-up of stratification during ebb (Fig. 6a). These contours are obtained from the high-resolution microstructure profiling, results of which are shown in Fig. 6c–f. The depth-mean salinity during flood and ebb is roughly symmetric, with incoming saline water during flood and outgoing fresher water during ebb. The behavior in temperature, in contrast, shows a distinct asymmetry in an event that occurred between 7 and 8 h: a sudden rise in temperature, especially near the bottom. Since water of this temperature arrives only hours later in the bulk of the water column, which is then also much more saline, it must be concluded that the earlier warm but relatively fresh peak belongs to another water mass, originating from the shallow parts of the basin

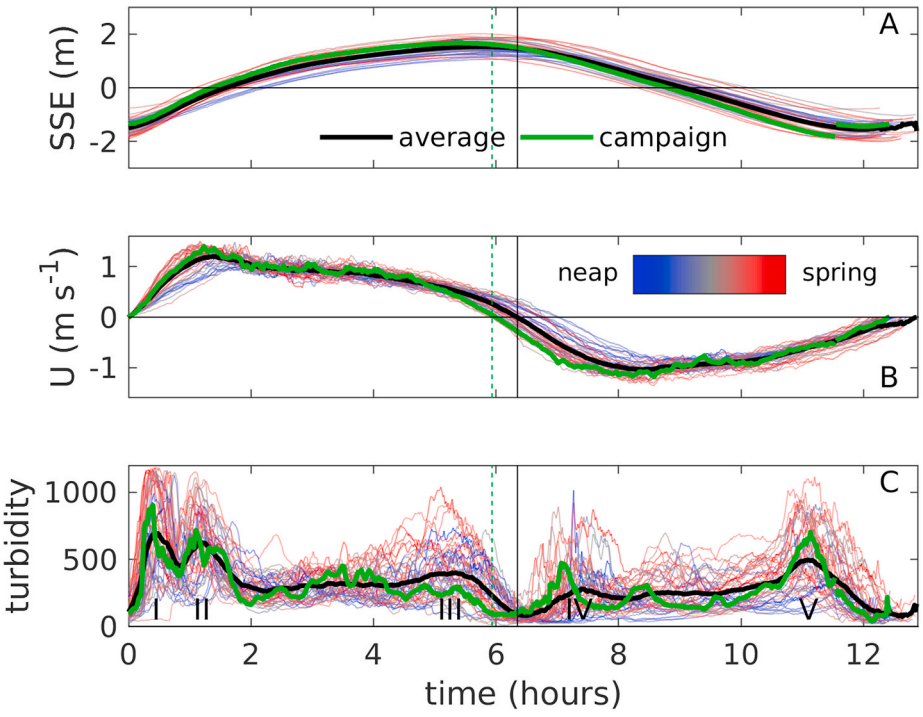

Fig. 5. (a) Sea surface elevation from tide gauge Knock, (b) depth-averaged along-channel current (positive values indicating flood), and (c) turbidity (in NTU), both from the long term mooring (yellow dot in Fig. 2a). Data is plotted for all recorded tidal cycles, aligned with the onset of flood and color-coded with the spring-neap cycle. The average over all tidal cycles is displayed in black; the tidal cycle that coincided with the one of the ship-based measurements is indicated in green. The vertical black line indicates the moment of slack tide from flood to ebb, averaged over all cycles; the same for the green dashed line, but then for the cycle of the ship-based measurements. (For interpretation of the references to color in this figure legend, the reader is referred to the Web version of this article.)

(probably from the harbour of Delfzijl) and advected to this spot by lateral circulation.

The presence of a strain-induced periodic stratification is further illustrated by the Brunt-Väisälä frequency N, here plotted as $\log_{10}N^2$ (Fig. 6e), along with turbulent dissipation ϵ in Fig. 6f. During slack tide after ebb, stratification increases significantly as turbulence decreases. The mid-water maximum stratification indicates a two-layer situation, generated by lateral exchange flow (see Fig. 6b). During early flood, this stratification is quickly eroded due to bottom-generated turbulence and along-current differential advection, such that the water column is fully mixed 2 h after slack tide. Later in the flood, the water column restratifies and turbulence reduces, probably due to lateral circulation and a weakening of the tidal current.

This flood-flow dynamics resembles the situation observed and numerically reproduced by (Purkiani et al., 2015) for the site near the channel slope of the Lister Deep. At slack water after ebb, the water column is stratified, and turbulence levels are low for some time. During flood, the stratification is subsequently eroded, but after a period of fully mixed conditions, restratification and strong turbulence damping sets in again. In the later flood phase, a balance between marginal stratification due to longitudinal differential advection and turbulent mixing seems to be established, a situation which is classically observed during ebb (Becherer et al., 2015). Overall, stratification is strong in the course of ebb till early flood, but weak in the course of flood till early ebb. However, the levels of turbulence are low around both slacks and high in the middle of both flood and ebb.

3.3. Suspended sediment concentrations

An overview of SPM concentrations through the tidal cycle is shown in Fig. 7a. The outstanding feature is the period of high concentrations during late ebb, which lasts about 2 h and involves the entire water column. The high turbidity was even visually noticeable from the ship, as 'clouds' of sediment were seen to drift towards the mouth of the estuary (Fig. 8). This period of high turbidity comes well after peak ebb velocities (about 2 h later), indicating the importance of advective effects in this region. The cloud of suspended sediment must originate from resuspension events that occurred further upstream.

These observations are confirmed by concurrent measurements carried out from another research vessel in the study area as part of *EDoM'18* (see Fig. 1, green dot): at this measurement site located 5 km upstream from our location, vertical profiling was carried out using a multisensor frame. The frame was (among others) equipped with a Seapoint turbidity meter (STM), used to derive SPM concentrations. The method to translate the optical backscatter data into SPM was comparable to the method described in section 2.3. At this location, too, a peak in SPM concentration peak during ebb is observed (Fig. 7c). There is also a peak during early flood, but it is more confined to the lower layer. Overall, the picture is qualitatively similar to the one at our site (Fig. 7a).

Some weaker peaks occur during early flood and early ebb, but they are confined to the near-bottom layer (see Fig. 7a) and hence contribute little to the overall suspended sediment mass. This is quantified by the black curve, representing the vertically integrated concentration. Again, the peak during late ebb stands out.

Zooming in on the near-bottom peaks, we show the data from the turbidity sensor mounted on the NIOZ mooring at a height of 0.34 m above the seabed (Fig. 7b). Here concentrations reach values as high as 2000 g m^{-3}. Interestingly, on the basis of this figure alone, one would expect a dominance of flood (since the peak during early flood is much higher than the one during late ebb), but we know from the ship-based measurements (Fig. 7a) that the opposite is the case if we consider the whole water column. (Incidentally, it should be noticed that the values occurring very close to the bottom are generally missed in ship-borne measurements, as the sensors do not quite get to this depth when lowered from the ship, because they are positioned higher on the frame. The samples from Niskin bottles, too, are typically obtained from a height of a few meters above the bottom.)

The onset of high turbidity at early flood in Fig. 7b is accompanied by a sudden rise in temperature, and by intense downslope currents Fig. 6b. This suggests the turbid water was originating from the channel to the port of Delfzijl; the sudden change in temperature was also recorded in the profiling data and the other mooring, within a time span of a few minutes.

Before turning to the tidally integrated transports of SPM, we first look at instantaneous fluxes by multiplying the current speed and the SPM concentration. The result is shown in Fig. 9, both for the along and

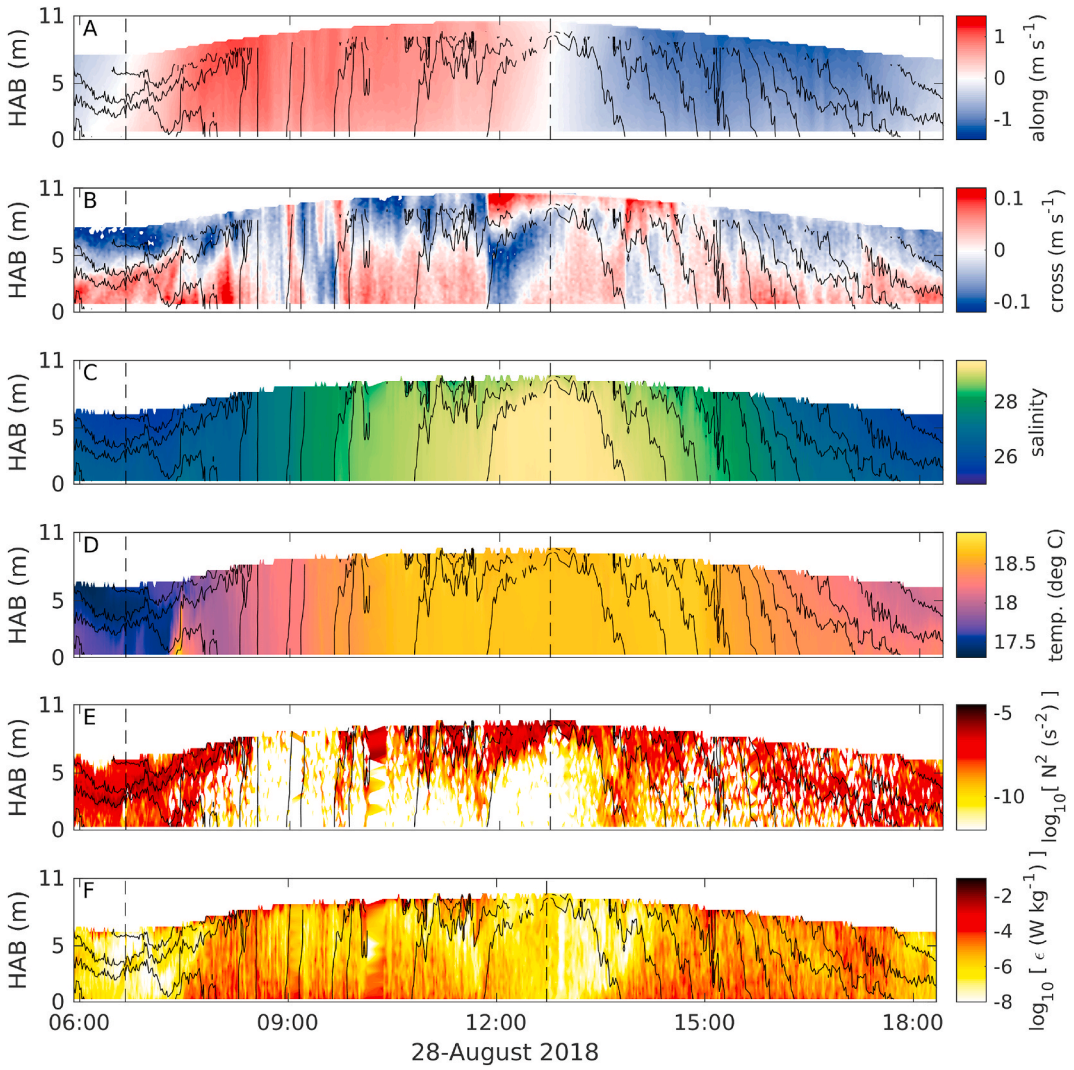

Fig. 6. Temporal evolution of (a) the along-channel current (flood in red, ebb in blue) and (b) cross-channel current (positive (red) = towards channel center, see Fig. 2a), measured with the ADCP on the NIOZ mooring. Panels (c) salinity, (d) temperature, (e) the Brunt-Väisälä frequency N (as $\log_{10}N^2$), and (f) the TKE dissipation rate, measured with the microstructure profiler from the R/V Navicula. Panels (e) and (f) are on a logarithmic scale. Black contour lines denote isopycnals in intervals of 0.25 kg m^{-3}. Vertical dashed lines indicate slack tides. Time is in UTC. (For interpretation of the references to color in this figure legend, the reader is referred to the Web version of this article.)

cross-slope directions. In the latter, a few periods with noticeable transport can be observed, namely at early flood and late ebb. In the along-slope direction, the ebb phase clearly is dominant, as already expected on the basis of the results in Fig. 7a.

3.4. Residual currents and SPM transport

Residual (i.e., tidally averaged) fluxes of water and SPM were calculated following (Klingbeil et al., 2019). This method takes into account the varying thickness of the water column and thus properly assigns a net value to each vertical position. For this, the current velocity from each ADCP as well as the SPM data were interpolated to 40 σ-coordinates (i.e., the water column is divided into 40 layers whose thickness deflates or inflates according to the movement of the free surface), keeping the constant time step of each individual ADCP.

For the calculation of the residual fluxes of water, we have three adjacent data sets available: the upward looking ADCPs on the two landers and the downward looking ship-borne ADCP (Fig. 2). They give similar results (Fig. 10a and b), allowing for the fact that the water depth at their deployment positions differs, which results in a vertical shift when plotting data with respect to height above bottom. Overall, there is a flood dominance in the lower part and a slight ebb dominance in the upper part (except for the ship-borne ADCP, which did not capture the near surface region). This is in line with the picture of the classical estuarine circulation. In the lateral (i.e., cross-channel) direction, there is a residual downslope current in the lower part, a counteracting residual flux in the middle of the water column, and another downslope component near the surface in the IOW mooring (the special beam angle of the ADCP deployed at the IOW mooring allowed for profiling up to the water surface, see section 2.2).

Turning now to residual SPM fluxes, it is no surprise (given the result from Fig. 9a) that they are overwhelmingly ebb dominant. All in all, a clear export of SPM is observed. The transport in the lateral direction is dominated by the combination of the steady two-layered lateral exchange flow in the second half of the ebb phase (Fig. 6b), when SPM concentrations were high throughout the water column: a cross-channel downslope transport of SPM in the lower part is compensated by a counteracting transport above.

3.5. Finer details in the lateral circulation

As described in the previous section, the tidally averaged lateral

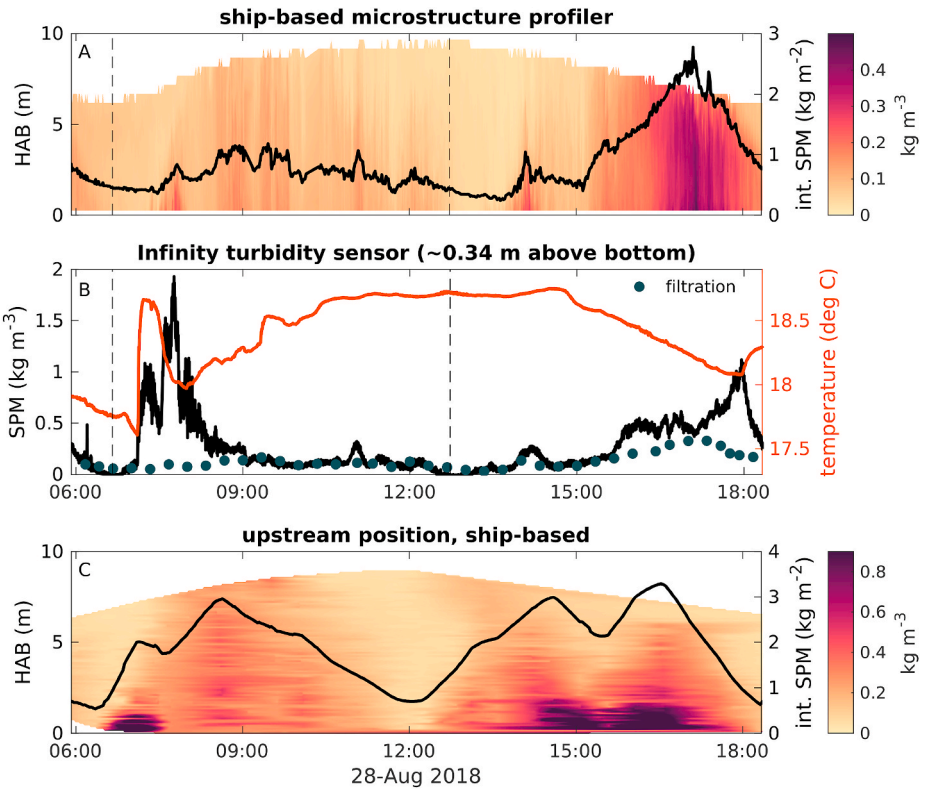

Fig. 7. (a) Temporal evolution of the SPM concentration, and the vertically integrated concentration (right vertical axis), obtained from microstructure profiling from the R/V Navicula. (b) SPM concentration (black line) and temperature (red line), recorded with the turbidity sensor on the NIOZ mooring; for comparison, SPM values from near-bottom Niskin samples are shown in gray dots; they were taken from the R/V Navicula. (c) Same as (a), but for the measurement position 5 km further upstream (the position of the green dot in Fig. 1). Vertical dashed lines denote the times of slack tide. Time is in UTC. (For interpretation of the references to color in this figure legend, the reader is referred to the Web version of this article.)

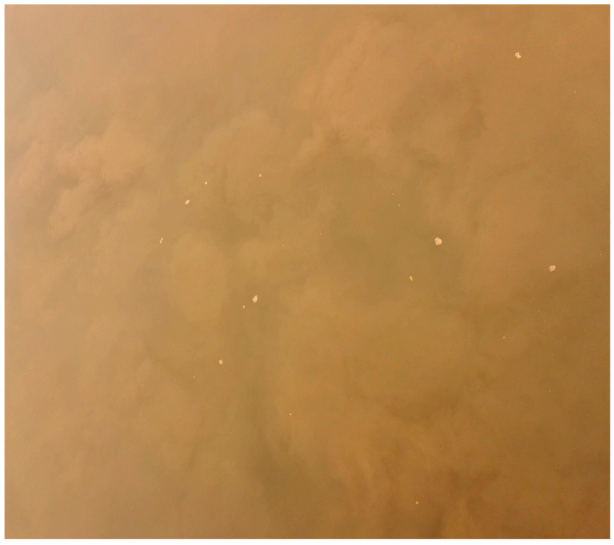

Fig. 8. Photograph made from the ship (at 16:52 UTC), showing clouds of sediment at the surface during the late-ebb turbidity peak.

circulation has mostly a two-layered structure, and is directed towards the deeper channel near the bottom, and towards the river bank near the surface (except closest to the river bank, where a near-surface flow towards the center of the channel is present; notice also that we cannot completely exclude the possibility that there is a three-layer structure in some cases that is not visible because of missing data at the top). A two-layered structure with this orientation is typical for the lateral circulation in curvature-dominated channels, but the intratidal variability appears to be more complex, and is investigated in detail in this section. We already noticed abrupt temporal changes in the lateral circulation in Fig. 6b. Now we add to this the spatial picture, which reveals small-scale differences in the patterns.

3.5.1. *Descriptive overview*

Representative lateral current structures for three phases of the tide (labeled I, III, V - note that these are *not* the same roman numerals as used to identify the SPM peaks in the context of Fig. 5) at the slope (red), central (green), and deep (orange) positions have been selected in Fig. 11.

Phase I (Fig. 11a) comprises the second half of ebb, during which the current is slackening. A two-layered circulation is visible throughout the sampled transect, directed towards the river bank at the surface and towards the deeper channel near the bottom. Maximum current velocities are in the order of 0.1 m s^{-1}.

At full flood, the lateral circulation becomes more variable and intermittent (phase II, not shown). After this, a steady circulation pattern is established after peak flood, labeled as state III. It is characterized by two circulation cells: the one on the slope is directed clockwise, the one at the deepest position counterclockwise. The lateral current at the central position is more variable, but mostly oriented as displayed in Fig. 11b.

Phase III is followed by a transitional phase, coinciding with the change from flood to ebb, where the lateral current structure is not persistent and shows strong spatial and temporal variability (phase IV, not shown). Finally, around peak ebb, we can identify a third steady state, referred to as phase V (Fig. 11c). It is characterized by spatially opposite circulation patterns.

To close the cycle, the transition between phases V and I happens abruptly. Over the slope, a bottom current directed towards the deeper channel evolves, followed by an acceleration of the along-channel ebb current at this position; right after that, the pattern of phase I is established again.

3.5.2. *Characterization by nondimensional numbers*

The dynamics in estuaries can be interpreted with the help of nondimensional numbers that quantify the relative importance of

different processes involved. We introduce these parameters here, as a guide to the interpretation of the various states of lateral circulation outlined in the previous section.

From U, the instantaneous water depth d and the instantaneous top-to-bottom buoyancy difference Δb, we calculate the (time-dependent) internal Froude number,

$$\mathrm{Fr} = \frac{U}{\sqrt{\Delta b d}} \tag{1}$$

(Seim and Gregg, 1997). For Froude numbers below a certain threshold (depending on vertical shear, radius of curvature and channel width, this threshold is approximately Fr = 5 in our case), stratification should suppress secondary circulation (Seim and Gregg, 1997). High Froude numbers up to Fr > 20 are present between approximately 08:30 and 09:50, i.e. during full flood when the water column is vertically homogeneous (see Fig. 6).

In well-mixed and weakly stratified estuaries, the lateral circulation is restricted by frictional forces rather than by vertical stratification. The nondimensional radius of curvature,

$$\widehat{R} = \frac{\sqrt{C_d}\kappa}{4}\frac{R}{D}, \tag{2}$$

with $\kappa = 0.41$ being the von Kármán constant, D the (mean) water depth, and using a typical radius of curvature of R = 6 km as indicated in Fig. 1 and a (nondimensional) drag coefficient of $C_d = 3 \times 10^{-3}$, is a measure for the relative importance of centrifugal and frictional forcing (Becherer et al., 2015). The relatively large value of $\widehat{R} = 3$ calculated for our data indicates a slight dominance of tidal mixing over curvature-induced lateral circulation.

The curvature Rossby number

$$\mathrm{Ro_c} = \frac{2u_A}{f\,R}, \tag{3}$$

where u_A is the amplitude of the tidal current velocity and f the Coriolis

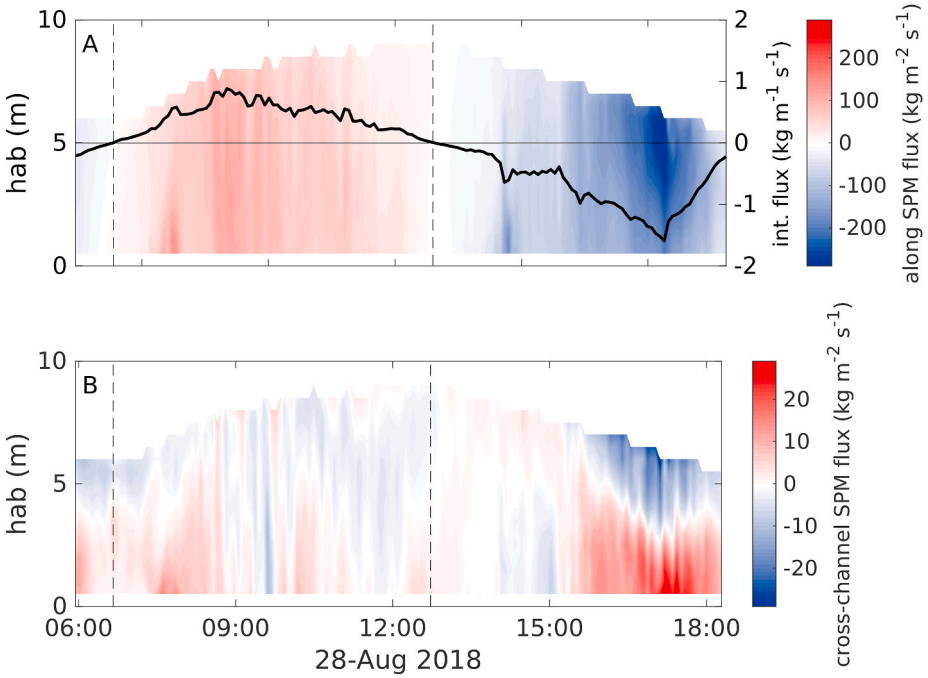

Fig. 9. SPM fluxes in the along and cross-slope directions through the tidal cycle. Based on the profiling and ship-borne ADCP data. Notice that the ranges differ in the colorbars. In (a), the black curve represents the vertically integrated SPM flux.

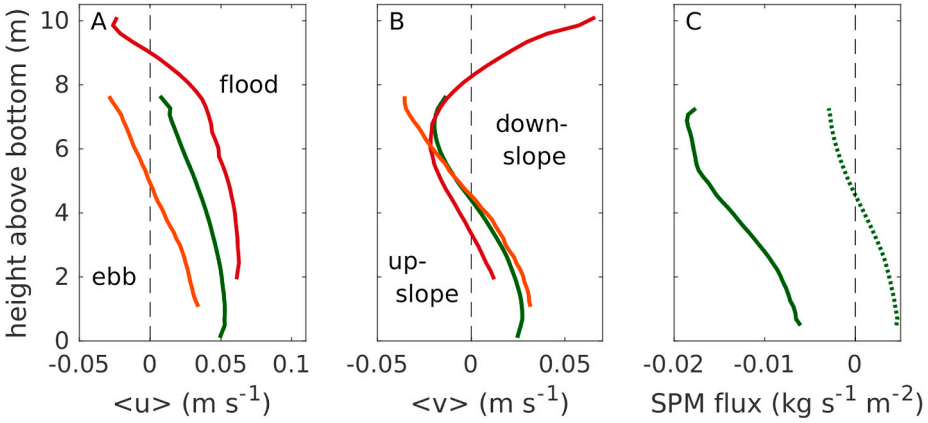

Fig. 10. Tidal average of the (a) along and (b) cross channel current. Colors indicate the different measuring positions, from shallow to deep (see Fig. 2 for reference): IOW mooring (red), Navicula (green), NIOZ mooring (orange). (c) Tidal average of the along (solid) and cross (dashed) channel SPM flux, at the central position. (For interpretation of the references to color in this figure legend, the reader is referred to the Web version of this article.)

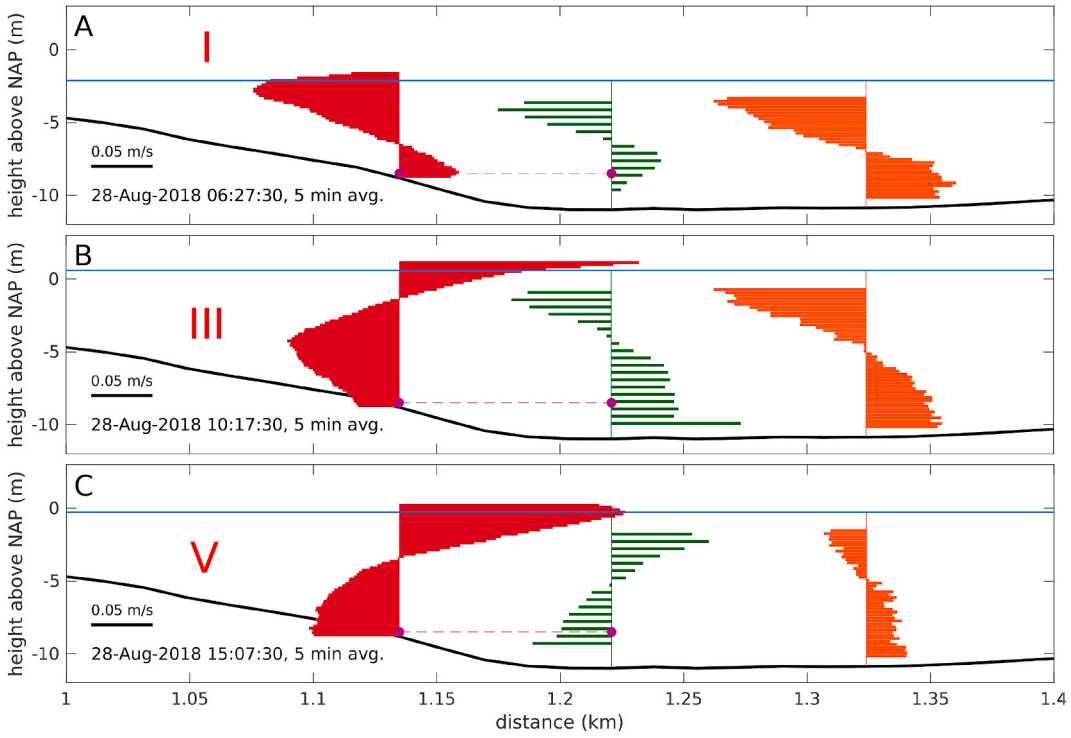

Fig. 11. (a)–(c) Three distinct steady phases of the cross-channel currents during the tidal cycle, labeled I, III and V. In each panel, from left to right, the cross-channel current profile measured by the IOW-mooring, research vessel, and NIOZ-mooring, respectively. The blue line indicates the water level (the bathymetric data sets underestimates the depth at the IOW mooring position), purple dots mark the positions for which the lateral density gradient is plotted in Fig. 12a. (For interpretation of the references to color in this figure legend, the reader is referred to the Web version of this article.)

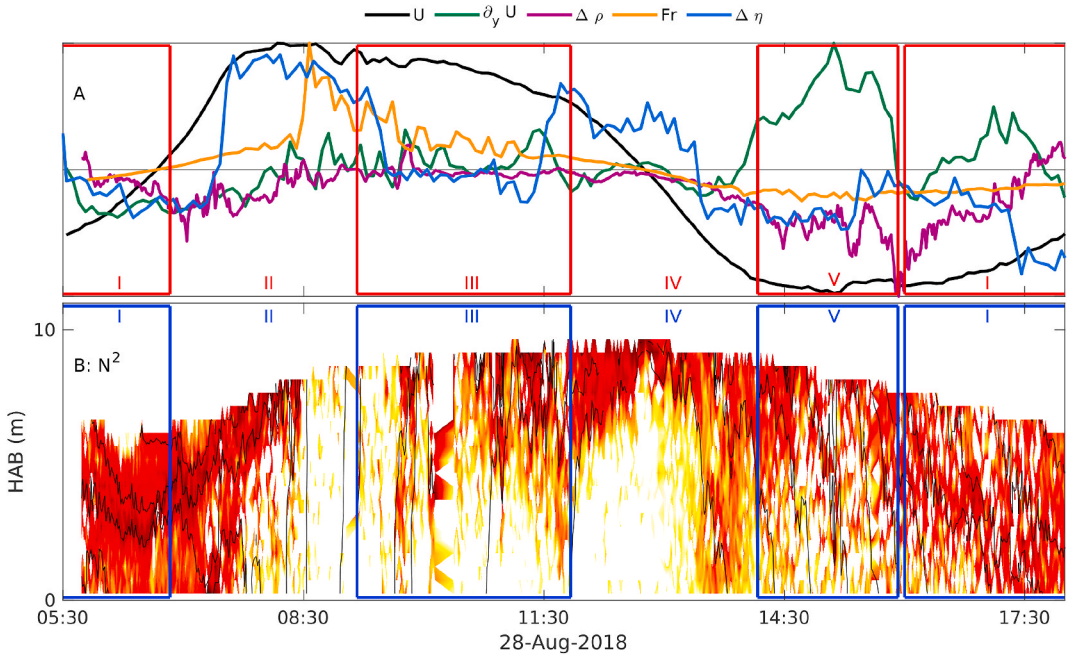

Fig. 12. (a) Depth-averaged along-channel current U (positives values = flood, black line), lateral shear $\partial_y U$ (green line, positive = higher at channel center), lateral density gradient between IOW mooring and ship (positive = higher values at mooring, purple line), Froude number (yellow line), relative pressure difference between the moorings (blue line). All data is normalized for better visibility. (b) Brunt-Väisälä frequency (reprint from Fig. 6). (For interpretation of the references to color in this figure legend, the reader is referred to the Web version of this article.)

frequency (Geyer, 1993), represents the relative importance of curvature compared to Coriolis effects (for smaller Ro_c, curvature effects become relatively less important). We find a value of $Ro_c = 2.6$, suggesting that curvature effects slightly dominate. In our case, curvature is expected to generate a lateral circulation directed towards the center of the channel near the bottom and towards the bank near the surface regardless of the tidal phase. However, we observe this kind of circulation only during the second half of ebb (phase I, Fig. 11a), and in the

deeper parts of the channel during phase III (Fig. 11b), suggesting that other mechanisms dominate during other phases of the tide. Lateral circulation patterns induced by Coriolis effects - which are expected to enhance the circulation pattern induced by curvature during flood, and counteract them during ebb phase - are not observed in the presented data set.

The importance of curvature effects for the generation of the lateral circulation at the measurement site is further supported by the *tidally-averaged* lateral current structure, which generally indicates a circulation oriented towards the center of the channel near the bottom, and towards the bank in the region above (Fig. 10b), typical for the lateral circulation in curvature-dominated channels (Einstein, 1926).

However, the Rossby number only indicates a slight dominance of centrifugal over Coriolis forcing, and the large nondimensional radius of curvature and the high Froude number indicate that tidal mixing has considerable impact on the lateral circulation, at least during some phases of the tidal cycle. In the following, the interplay between the lateral circulation and the vertical stratification will be analyzed.

To understand the temporal evolution of the lateral circulation, available lateral gradients and other helpful data are displayed in Fig. 12a: The along-channel current U, averaged over all three available ADCPs; the difference in depth-averaged along-channel flow between the ADCP on the IOW mooring (closest to the river bank) and the average over all ADCPs, labeled $\partial_y U$, as a measure for the strength of cross-channel shear; the Froude number; the relative pressure difference between the ADCPs in both moorings $\Delta\eta$; and the horizontal density difference between the CTD on the IOW mooring and the ship-based measurements at the same depth. As all moorings and the ship were located within a radius of less than 200 m, gradients are generally small and might not represent the overall cross-channel gradients well, as they can be affected by small scale processes: The near bottom density gradient $\Delta\rho$, for example, is created not only by differential advection, but also mirrors the effect of the lateral circulation on the redistribution of buoyancy. Due to the different offset in the pressure sensors between the respective ADCPs and the uncertainty of the real bottom depth, the lateral pressure gradient $\Delta\eta$ can only be regarded as the relative change of the lateral sea level slope, not the absolute difference.

The spatial proximity of the moorings and the very small and therefore less accurate gradients make a quantitative analysis uncertain. All quantities displayed in Fig. 12a are therefore normalized for a better qualitative comparison.

In Fig. 12, representative lateral current structures for three phases of the tide are indicated as I, III, and V (as in Fig. 11), with intermediate transitional phases II and IV.

Starting with phase I (at the *end* of the measurement period, Fig. 12a), which comprises the second half of ebb, when the current magnitude is decreasing again after full ebb: A steady exchange flow in the orientation as expected for curved channels (directed towards the river bank at the surface and towards the deeper channel near the bottom) has developed (Fig. 11a). Slightly enhanced lateral shear in the along-channel direction (green line) causes a decrease in near-bottom density at the ship position, while the density at the IOW mooring remains approximately constant. Assuming that this lateral baroclinic density gradient is established over a greater cross-channel distance, it would reinforce the lateral circulation pattern driven by centrifugal forces. The lateral circulation pattern is, however, present *before* the rise of the lateral density gradient, indicating that the main driving force during this phase is the channel curvature, reinforced by differential advection.

At the beginning of phase II, after slack tide, a lateral surface return flow towards the channel center develops at the position of the IOW mooring, which might also be present but not captured by the other two current profilers, which do not cover the very near surface area. Vertical stratification (Fig. 12b) is eroded due to enhanced turbulence (see section 3.2) starting from the sea bed. The lateral surface return flow from the bank toward the channel might advect less dense water and help to maintain the surface stratification in the first half of phase II. A lateral pressure gradient is established at 7:30 h, potentially driven by curvature and amplifying Coriolis effect during the increasing flood current. The pattern of the lateral circulation changes drastically when the Froude number increases at 8:30 h: the water column is now well-mixed, and the flow becomes more unsteady. Still small but enhanced variability in the main flow direction might indicate the presence of advected small scale eddies that modify the tidal current.

During phase III, when the flood current is slowly decelerating, the upper part of the water column is restratified, and the Froude number as well the barotropic pressure gradient decrease. Two circulation cells are formed: the one on the slope is directed clockwise, the one at the deepest position counterclockwise. The lateral current at the ship position is more variable, but mostly oriented as displayed in Fig. 11b. From the ship, which was positioned approximately in the convergence zone of these two cells at the surface, a restratification of the upper water layer from the top is observed, while turbulence is still comparably high. The surface convergence of the two cells could be an explanation for this restratification. The immediate stop of the deepening of the stratified surface zone that coincides with the breakdown of the cell convergence at the end of phase III supports this hypothesis.

While the counterclockwise circulation in the deeper part can be explained by curvature effects, the observed density gradient (Fig. 12a, purple line) is close to zero and does therefore not support the formation of the clockwise circulation cell on the slope. However, the slope and central position are less than 100 m apart, and the lower part of the water column (where the measurements were performed) is still well-mixed; and a stronger salinity gradient further up the slope could be formed by differential advection. In this case, the resulting baroclinic pressure gradient may trigger the formation of the observed two-layered current near the slope. By lack of corroborating evidence, this is of course speculative. Lateral shear in the along-channel flow (flood current deceleration is first observed at the NIOZ mooring, then at the ship, and last at the IOW mooring closer to the bank) drives the subsequent rise of the lateral pressure gradient at 11:15 h.

The peak of the lateral barotropic pressure gradient marks the beginning of phase IV. Triggered by the high pressure gradient, the exchange flow at the position of the NIOZ mooring changes orientation, so that (temporarily) one clockwise circulation cell is formed. During the transition from flood to ebb phase, the lateral barotropic pressure gradient decreases (or is even reversed), suggesting that Coriolis forcing during ebb now counteracts the pressure gradient induced up by curvature effects.

During phase V (full ebb), the lateral shear in along-channel flow is high, as the along-channel current at the IOW mooring is not accelerating along with the ebb current further into the channel during phase V. A strong exchange flow - directed towards the bank near the bottom and towards the channel near the surface, possibly caused by Coriolis effects - is present at the IOW mooring near the bank and less pronounced at the ship position, and a weaker counterclockwise circulation is observed at the NIOZ mooring side (Fig. 11c). Even though the along-channel velocities near the center of the channel are higher, the lateral density gradient is decreasing (as the density at the IOW mooring is decreasing faster than at the ship), opposite to the behaviour expected for the observed lateral shear and for differential advection during ebb current in general. The (faster) decrease in density observed at the IOW mooring is therefore rather caused by the strong lateral near bottom current, which transports denser water from the deeper center of the channel up the slope towards the shoal.

At the end of phase V, the circulation pattern observed at the NIOZ mooring changes direction and the lateral circulation pattern typical for phase I is established.

4. Discussion and conclusions

The measurement campaign described in this article took place on a

day with very weak winds and low river run-off. Thus, the state was as close as one may practically get to "tides-only". Previously, such a state was modelled by Ridderinkhof (1997). He found a net import of suspended sediment due to tidal asymmetries formed by the combination of the tidal constituents M2, M4 and M6. We find the opposite (i.e., a net export), but this contradiction can be traced back to an assumption in the model, namely spatial uniformity in the availability of sediment. In reality, areas of high turbidity are found more inward in the basin, which acts as a source region for transport.

We describe the conditions of our campaign as nearly ''tides-only'', but with the proviso that there may be a memory in the system. This is suggested by the fact that the first low water was half a meter higher than the second; the first one is possibly an anomaly due to westerly winds on the previous day (see end of Section 2.1). Stronger winds would not only cause wave-induced resuspension, but (depending on the direction) may also create higher water levels implying that tidal flats remain inundated and subject to erosion for a longer period. The wind was previously pointed to as an important factor in SPM transport in the Ems estuary by De Jonge et al. (1995) and De Jonge and Van Beusekom (1995).

The site of our campaign was at the southern part of the channel and we cannot infer from our measurements whether a net export of SPM also occurred elsewhere across the channel (see, e.g., Becherer et al. (2016), who also found an export during calm periods, due to tidal pumping, while asymmetries may occur in the curved channel). Yet, visual evidence of high SPM concentrations during ebb (as in Fig. 8) stretched well beyond our measurement site, strongly suggesting that this was not just a local phenomenon.

Based on a comparison with a nearby lander, located there during a month, we conclude that the general characteristics of our measurements during one tidal cycle are in line with those during the rest of the month. During other parts of the year (not covered here), conditions are of course very different, with stronger winds and more run-off much of the time. Only by repeating the measurement campaign can their effect on sediment transport be assessed. We expect that high run-off conditions, implying enhanced estuarine circulation, may be more favorable to import of sediment. In any case, there must be periods of import (compensating the export observed here) or else there would be no turbidity problem in the Ems. Like in other parts of the Wadden Sea (see, e.g. Sassi et al. (2015)), the picture that arises is one of high variability in the tidally-averaged SPM transports, even in direction, depending on wind conditions or fresh-water run-off. The challenge remains to evaluate the long-term cumulative effect of these variable transports in estuaries. The variability includes tidal asymmetries associated with stratification and sediment resuspension, as studied by McSweeney et al. (2016) in deployments across Delaware Estuary and continued for several months. In this respect, even an intensive campaign as the present one cannot be conclusive as it covered only one tidal cycle.

In the interpretation of the data from our measurement campaign, we can distinguish between the overall picture and the finer details. The overall picture is dominated by the pronounced high concentrations of SPM during late ebb (Fig. 7a) and a resulting net export (Fig. 10c), which occurs throughout the water column and consistently during the course of several hours. Based on the data at our location, it cannot be concluded whether the SPM actually leaves the estuary further downstream or stays in the basin, as a relocation of a turbidity peak adjusting to the present (tide-only) conditions.

This stands in contrast to what we may call the "finer details", which are seemingly momentous but actually have little effect on the overall picture. One of these phenomena is the occurrence of occasional high turbidity peaks observed in the bottom landers (Fig. 7b). For the overall transport, they are insignificant because the high concentrations are present only in a very small portion of the water column, and hence involve a comparatively small sediment mass. Moreover, being very close to the bottom, they occur at a place where currents are weak, which further diminishes their role in the overall sediment transport.

Another finding is the extraordinarily complex nature of the lateral circulation. It is characterized not only by abrupt transitions during a tidal cycle, but also involves a large degree of spatial variability, even within the small distance between our deployments, which were less than 200 m apart. This small-scale variability, revealed in Fig. 11, poses a challenge for both fieldwork campaigns and numerical modelling work. The high spatial resolution we had at our measurement location can of course not be sustained when one covers wider areas (e.g., a full cross-channel transect). But this inevitably means that the high spatial variability is no longer covered, and, more seriously, that the measurements one does have are unlikely to be representative for the cross section as a whole. For numerical modelling, too, it poses a formidable challenge to resolve the dynamics at such a small spatial scale (we note that lateral dynamics at the full cross-channel scale can be captured by models, as in, e.g., Zhou et al. (2020), who identified a new mechanism for tidal straining circulation). The reassuring aspect, though, is that the overall transport of SPM in the along-channel direction was robust and did not show such a spatial and temporal variability.

CRediT authorship contribution statement

Kirstin Schulz: Investigation, Validation, Writing - original draft, Writing - review & editing. **Hans Burchard:** Conceptualization, Writing - review & editing, Funding acquisition. **Volker Mohrholz:** Investigation. **Peter Holtermann:** Investigation. **Henk M. Schuttelaars:** Conceptualization, Writing - review & editing. **Marius Becker:** Investigation. **Christian Maushake:** Investigation. **Theo Gerkema:** Conceptualization, Writing - review & editing, Funding acquisition.

Declaration of competing interest

The authors declare that they have no known competing financial interests or personal relationships that could have appeared to influence the work reported in this paper.

Acknowledgements

The findings in this manuscript represent the first results from the EDoM'18 project, a joint field campaign following an initiative by Rijkswaterstaat, Deltares (The Netherlands), the Federal Waterways and Shipping Administration and the BAW - Federal Waterways Engineering and Research Institute (Germany); shiptime and funding was provided by the participating institutes. We gratefully acknowledge the Lower Saxony Water Management, Coastal Defence and Nature Conservation Agency (NLWKN) and the Water and Shipping Administration (WSA Ems-Nordsee) for providing longterm monitoring data. We thank the crews of R/V *Navicula*, and GMS *Friesland* (operated by WSA Ems-Nordsee), and Claudia Morys and Toralf Heene for their help with the measurements. We additionally thank Wouter Kranenburg for helpful discussions. Funding for K. Schulz was provided by the TTW project "Sediment for the salt marshes: physical and ecological aspects of a mud motor" (grant number 13888). M. Becker is funded by Kiel Marine Science (KMS). The work at IOW was carried out in the framework of the Research Training Group Baltic TRANSCOAST GRK 2000 funded by the German Research Foundation. We thank two anonymous reviewers for their helpful comments. While working on the revision, we learnt with profound sadness that the third reviewer, Victor de Jonge, had passed away. In him, we have lost a convivial colleague and a high-spirited expert on estuaries.

Appendix A. Supplementary data

Supplementary data to this article can be found online at https://doi.org/10.1016/j.ecss.2020.106902.

References

Becherer, J., Stacey, M.T., Umlauf, L., Burchard, H., 2015. Lateral circulation generates flood tide stratification and estuarine exchange flow in a curved tidal inlet. J. Phys. Oceanogr. 45 (3), 638–656.

Becherer, J., Flöser, G., Umlauf, L., Burchard, H., 2016. Estuarine circulation versus tidal pumping: sediment transport in a well-mixed tidal inlet. J. Geophys. Res. 121, 1–20. https://doi.org/10.1002/2016JC011640.

Burchard, H., Schuttelaars, H.M., Ralston, D.K., 2018. Sediment trapping in estuaries. Ann. Rev. Mar. Sci. 10, 371–395.

Chernetsky, A.S., Schuttelaars, H.M., Talke, S.A., 2010. The effect of tidal asymmetry and temporal settling lag on sediment trapping in tidal estuaries. Ocean Dynam. 60, 1219–1241.

Cox, T.J.S., Maris, T., Van Engeland, T., Soetaert, K., Meire, P., 2019. Critical transitions in suspended sediment dynamics in a temperate meso-tidal estuary. Sci. Rep. 9 (1), 12745.

De Jonge, V.N., Schückel, U., 2019. Exploring effects of dredging and organic waste on the functioning and the quantitative biomass structure of the Ems estuary food web by applying Input Method balancing in Ecological Network Analysis. Ocean Coast. Manag. 174, 38–55.

De Jonge, V.N., 1995. Wind-driven tidal and annual gross transport of mud and microphytobenthos in the Ems Estuary, and its importance for the ecosystem. In: Dyer, K.R., Orth, R.J. (Eds.), Changes in Fluxes in Estuaries. Olsen & Olsen, pp. 29–40.

De Jonge, V.N., Schuttelaars, H.M., Beusekom, J.E.E., Talke, S.A., De Swart, H.E., 2014. The influence of channel deepening on estuarine turbidity levels and dynamics, as exemplified by the Ems estuary. Est. Coast Shelf Sci. 139, 46–59.

De Jonge, V.N., Van Beusekom, J.E.E., 1995. Wind- and tide-induced resuspension of sediment and microphytobenthos from tidal flats in the Ems estuary. Limnol. Oceanogr. 40 (4), 766–778.

Dijkstra, Y.M., Schuttelaars, H.M., Schramkowski, G.P., Brouwer, R.L., 2019a. Modeling the transition to high sediment concentrations as a response to channel deepening in the Ems river estuary. J. Geophys. Res.: Oceans 124 (3), 1578–1594.

Dijkstra, Y.M., Schuttelaars, H.M., Schramkowski, G.P., 2019b. A regime shift from low to high sediment concentrations in a tide-dominated estuary. Geophys. Res. Lett. 46 (8), 4338–4345.

Einstein, A., 1926. Die Ursache der Mäanderbildung der Flußläufe und des sogenannten Baerschen Gesetzes. Naturwissenschaften 14 (11), 223–224.

Gerkema, T., Nauw, J.J., Van der Hout, C.M., 2014. Measurements on the transport of suspended particulate matter in the Vlie Inlet. Neth. J. Geosci. 93 (3), 95–105.

Geyer, W.R., 1993. Three-dimensional tidal flow around headlands. J. Geophys. Res.: Oceans 98 (C1), 955–966.

Klingbeil, K., Becherer, J., Schulz, E., De Swart, H.E., Schuttelaars, H.M., Valle-Levinson, A., Burchard, H., 2019. Thickness-weighted averaging in tidal estuaries and the vertical distribution of the Eulerian residual transport. J. Phys. Oceanogr. 49 (7), 1809–1826.

McSweeney, J.M., Chant, R.J., Sommerfield, C.K., 2016. Lateral variability of sediment transport in the Delaware Estuary. J. Geophys. Res. Oceans 121, 725–744.

Purkiani, K., Becherer, J., Flöser, G., Gräwe, U., Mohrholz, V., Schuttelaars, H.M., Burchard, H., 2015. Numerical analysis of stratification and destratification processes in a tidally energetic inlet with an ebb tidal delta. J. Geophys. Res.: Oceans 120 (1), 225–243.

Ridderinkhof, H., 1997. The effect of tidal asymmetries on the net transport of sediments in the Ems-Dollard estuary. J. Coast Res. 25, 41–48.

Sassi, M., Duran-Matute, M., Van Kessel, T., Gerkema, T., 2015. Variability of residual fluxes of suspended sediment in a multiple tidal-inlet system: the Dutch Wadden Sea. Ocean Dynam. 65 (9–10), 1321–1333.

Schulz, K., Gerkema, T., 2018. An inversion of the estuarine circulation by sluice water discharge and its impact on suspended sediment transport. Est. Coast Shelf Sci. 200, 31–40.

Schuttelaars, H.M., De Jonge, V.N., Chernetsky, A., 2013. Improving the predictive power when modelling physical effects of human interventions in estuarine systems. Ocean Coast. Manag. 79, 70–82.

Seim, H.E., Gregg, M.C., 1997. The importance of aspiration and channel curvature in producing strong vertical mixing over a sill. J. Geophys. Res.: Oceans 102 (C2), 3451–3472.

Simpson, J.H., Brown, J., Matthews, J., Allen, G., 1990. Tidal straining, density currents, and stirring in the control of estuarine stratification. Est. Coasts 13 (2), 125–132.

Talke, S.A., De Swart, H.E., Schuttelaars, H.M., 2009. Feedback between residual circulations and sediment distribution in highly turbid estuaries: an analytical model. Cont. Shelf Res. 29, 119–135.

Van Beusekom, J.E.E., De Jonge, V.N., 1998. Retention of phosphorus and nitrogen in the ems estuary. Estuaries 21, 527–539.

Van Maren, D.S., Oost, A.P., Wang, Z.B., Vos, P.C., 2016. The effect of land reclamations and sediment extraction on the suspended sediment concentration in the Ems estuary. Mar. Geol. 376, 147–157.

Zhou, J., Stacey, M.T., Holleman, R.C., Nuss, E., Senn, D.B., 2020. Numerical investigation of baroclinic channel-shoal interaction in partially stratified estuaries. J. Geophys. Res. Oceans 125, 1–18. https://doi.org/10.1029/2020JC016135.